Article

Evaluation of CYGNSS Observations for Flood Detection and Mapping during Sistan and Baluchestan Torrential Rain in 2020

Mahmoud Rajabi *, Hossein Nahavandchi[ID] **and Mostafa Hoseini**[ID]

Department of Civil and Environmental Engineering, Norwegian University of Science and Technology NTNU, 7491 Trondheim, Norway; hossein.nahavandchi@ntnu.no (H.N.); mostafa.hoseini@ntnu.no (M.H.)
* Correspondence: mahmoud.rajabi@ntnu.no; Tel.: +47-92332254

check for updates

Abstract: Flood detection and produced maps play essential roles in policymaking, planning, and implementing flood management options. Remote sensing is commonly accepted as a maximum cost-effective technology to obtain detailed information over large areas of lands and oceans. We used remote sensing observations from Global Navigation Satellite System-Reflectometry (GNSS-R) to study the potential of this technique for the retrieval of flood maps over the regions affected by the recent flood in the southeastern part of Iran. The evaluation was made using spaceborne GNSS-R measurements over the Sistan and Baluchestan provinces during torrential rain in January 2020. This area has been at a high risk of flood in recent years and needs to be continuously monitored by means of timely observations. The main dataset was acquired from the level-1 data product of the Cyclone Global Navigation Satellite System (CYGNSS) spaceborne mission. The mission consisted of a constellation of eight microsatellites with GNSS-R sensors onboard to receive forward-scattered GNSS signals from the ocean and land. We first focused on data preparation and eliminating the outliers. Afterward, the reflectivity of the surface was calculated using the bistatic radar equations formula. The flooded areas were then detected based on the analysis of the derived reflectivity. Images from Moderate-Resolution Imaging Spectroradiometer (MODIS) were used for evaluation of the results. The analysis estimated the inundated area of approximately 19,644 km^2 (including Jaz-Murian depression) to be affected by the flood in the south and middle parts of the Sistan and Baluchestan province. Although the main mission of CYGNSS was to measure the ocean wind speed in hurricanes and tropical cyclones, we showed the capability of detecting floods in the study area. The sensitivity of the spaceborne GNSS-R observations, together with the relatively short revisit time, highlight the potential of this technique to be used in flood detection. Future GNSS-R missions capable of collecting the reflected signals from all available multi-GNSS constellations would offer even more detailed information from the flood-affected areas.

Keywords: CYGNSS; flood detection; Sistan and Baluchestan; flood mapping; GNSS-R

1. Introduction

Natural disasters are the reason for many serious disturbances to communities and the environment. There have been many human, environmental, social, and economic losses, which are beyond the power of the community to tolerate [1]. Floods have been considered as one of the most catastrophic events, causing extensive damage to the artificial and natural environment and devastation to human settlements [2]. Economic losses due to the effects of damaging floods have increased significantly around the world [3]. Flooding happens when water bodies overflow riversides, lakes, dams, or dikes in low-lying lands during heavy rainfall [4]. The higher temperature at the Earth's surface leads to

increased evaporation and greater overall precipitation [5]. Increased precipitation, although associated with inland flooding, can also increase the risk of coastal flooding [6].

Flood detection, and subsequently, produced maps, are beneficial in two important phases: During the flood, when we need emergency management planning, and after the flood, for land use planning, defining construction standards, and damage assessment [7]. Heavy precipitation has led floods to occur more frequently in different countries, which have drawn considerable attention over the past years. There are many regions of Iran affected by floods, for instance, heavy rainfall from mid-March to April 2019 led to flooding in 28 of 31 provinces, with the most severe flooding occurring in Golestan, Fars, Khuzestan, and Lorestan [8]. The recent torrential rain in mid-January 2020 in the southeastern region of Iran caused a devastating flood in the Sistan and Baluchestan province. We investigated the latter case in this study.

Land surveying and airborne observations are the traditional methods for flood detection, but when when flood detection is conducted on a large scale, these methods are costly and slow. Space-based Remote Sensing (RS) can be considered as a practical alternative that provides up-to-date information from various sensors that have been onboard different satellites. However, there are some limitations in using RS data products for the study of flooding. For instance, optical RS can have its limitations during severe weather conditions and during night. Therefore, in some cases before and after a flood event, the optical RS imagery does not provide the required information [7]. Radar RS in the microwave spectrum can surpass these restrictions because the wave can penetrate clouds and vegetation and can effectively work at night. Among the several radars RS sensors currently in operation, Synthetic Aperture Radar (SAR) imagery provides high spatial resolution data which is typically based on a monostatic configuration. However, the revisit time of satellites with the configuration of the monostatic radar (single satellites), like SAR, is long (more than one week) and cannot offer the desirable continuous high temporal resolution for flood detection purposes. Accordingly, owing to the highly dynamic nature of the flood, SAR images are not used operationally during floods [9–11].

The primary services of the Global Navigation Satellite System (GNSS) are positioning, navigation, and timing. Besides, many other applications, including GNSS RS, have been introduced in recent decades. Measurements made by GNSS RS techniques provide valuable information about different components of the Earth system. Observations of the GNSS signals passing through the atmosphere have been employed to study the atmospheric layers and their variabilities [12,13]. GNSS signals after reflection from the Earth's surface can also provide information about the reflecting surface. These reflections have been used to study various parameters of the Earth's surface and water cycles, such as snow depth [14], ice height and sea level [15], soil moisture [16], vegetation [17], flood [11,18], ocean eddies [19], wind speed [20], salinity [21], etc.

Global Navigation Satellite System Reflectometry (GNSS-R) is an innovative technique aimed at deriving geophysical parameters by analyzing GNSS signals reflected off the Earth's surface in a bistatic geometry. This technique is an efficient microwave remote sensing approach that utilizes transmitted navigation signals as sources of opportunity. Numerous GNSS satellites, including GPS, Galileo, GLONASS, and Bei-Dou/Compass, are currently transmitting navigation signals based on spread-spectrum technology. Thus, a constellation of GNSS-R small satellites, at a lower cost compared to ordinary RS satellites, can provide a much shorter revisit time using low-cost, low-power passive sensors. Many earlier studies have introduced the applications of GNSS-R on the oceans, land, and ice [22–24].

The soil moisture, surface roughness, vegetation, and topography are parameters which affect microwave signals. GNSS-R signals as a bistatic radar are also affected by those parameters [25]. However, GNSS signals are at the L-band, which is ideal for soil moisture and surface water remote sensing due to the higher capacity to penetrate vegetation compared to shorter wavelengths [16]. In addition, this technique uses the bistatic configuration, which has a lower sensitivity to surface roughness relative to monostatic [26]. The signals reflected off the surface have a direct relation with

surface water and moisture content [11]. For example, the rise of soil moisture leads to increase the signal strength. Using this mechanism could contribute to detecting soil saturation, flooded area, and inland water.

The Cyclone Global Navigation Satellite System (CYGNSS) mission is a constellation of eight microsatellites, each with a GNSS-R receiver onboard. The receiver can track and process four GPS signals simultaneously. The tracked GPS L1 C/A signals after reflection from the Earth's surface are used to produce Delay Doppler Maps (DDMs). The overall median revisit time is 2.8 h, and the mean revisit time is 7.2 h [27]. Theoretically, the footprint of reflection received by CYGNSS is nearly 0.5 km × 0.5 km. For the ocean, which has a very rough surface, the spatial resolution is approximately 25 km × 25 km [28,29]. Table 1 shows CYGNSS microsatellite parameters retrieved from [16,23]. The main mission of CYGNSS is to measure the ocean surface wind speed in hurricanes and tropical cyclones, so a relatively low orbital inclination was designed for the satellites. CYGNSS continuously makes measurements over the oceans and provides useful information over the land [29]. CYGNSS offers distinct features compared to other remote sensing techniques such as optical and active monostatic radar. It uses a passive sensor at the L-band frequency wave, which works in all weather conditions regardless of the time of the day, i.e., it can penetrate clouds, fog, rain, storms, and vegetation, and works at night, unlike optical sensors. The CYGNSS constellation of eight microsatellites provides a relatively short revisit time with global coverage over equatorial regions. The products of CYGNSS are publicly available over the oceans and land.

Table 1. The Cyclone Global Navigation Satellite System (CYGNSS) satellite parameters.

Parameters	Description
Orbit	LEO, ~520 km, Nonsynchronous
Period	95.1 min
Spatial Resolution	~25 km × 25 km (incoherent), ~0.5 km × 5 km (coherent, theoretical)
Revisit Times	2.8 h median, 7.2 h mean
Polarization of the reflectometry antennas	LHCP
Coverage	−38 < Latitude < 38 & −180 < Longitude < 180
Type of Data which is relevant	Observe GPS L1 C/A signals and Delay Doppler Maps

Radar remote sensing for soil moisture retrieval and surface water detection is common using both monostatic [7,30] and bistatic geometry. The sensitivity of spaceborne GNSS-R (as a bistatic radar) to surface water and soil moisture has been widely studied [11,16,18,23,31–33]. Most of the studies have used observations from ground-based or space-based receivers, e.g., CYGNSS or Technology Demonstration Satellite-1 (TDS-1). Observational evidence demonstrates that GNSS-R is highly sensitive to inland surface waters, e.g., lakes and rivers [34].

Sistan and Baluchestan is one of the driest regions of Iran, with a slight increase in rainfall from east to west, and is a province at a high risk of flooding. The aim of this study was to indicate the capability of spaceborne GNSS-R for detecting and mapping of flood in the south part of Iran. The methodology for preparing and processing data is the same as those used described by the authors of [16,18].

2. Study Area

The Sistan and Baluchestan province is located in the east and southeast of Iran (58°55′–63°20′ E longitude and 25°04′–31°25′ N latitude), bordering Pakistan and Afghanistan, and its capital is Zahedan. This province is the second largest province in Iran with an area of 180,726 km^2 and a population of about 2.5 million. Figure 1A shows the location of this province on the Maphill Earth map. There is a depression in the study area known as the Hamun-Jaz-Murian basin, which is part of the central plateau basin. This basin is located in the southeast of Iran between 56°17′ and 61°25′ E longitude and 26°32′ and 29°35′ N latitude (Figure 1B). Its total area is about 69,390 km^2, of which 44% is mountains. The depression belongs to Kerman and Sistan-Baluchistan provinces [35]. Figure 1C shows a flooded region in IranShahr, which is one of the cities in this province.
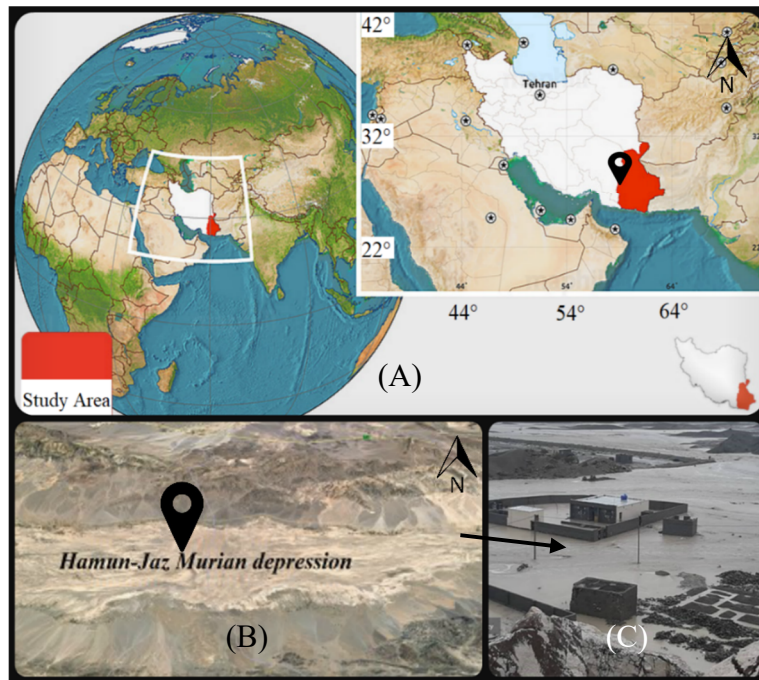
Figure 1. (**A**) The red region shows the location of the Sistan and Baluchestan province in the southeast of Iran, which is our study area. (**B**) The Hamun Jaz-Murian depression, which is located between the Kerman and Sistan and Baluchestan provinces. (**C**) IranShahr, one of the flooded cities in the study area.

Sistan and Baluchestan is one of the warmest regions in Iran, with a desert climate and an average daily temperature of 29 degrees centigrade. For several months of the year, it is warm at temperatures continuously above 25 degrees centigrade, and temperatures sometimes exceed above 40 degrees centigrade. Figure 2 illustrates the average precipitation per day over 20 years. As can be seen, 0.40 mm/day rainfall is normal during January in the province, but between 10 January and 12 January 2020, this amount is over 100 mm. Figure 3 shows the precipitation rate from 8 January to 13 January 2020.
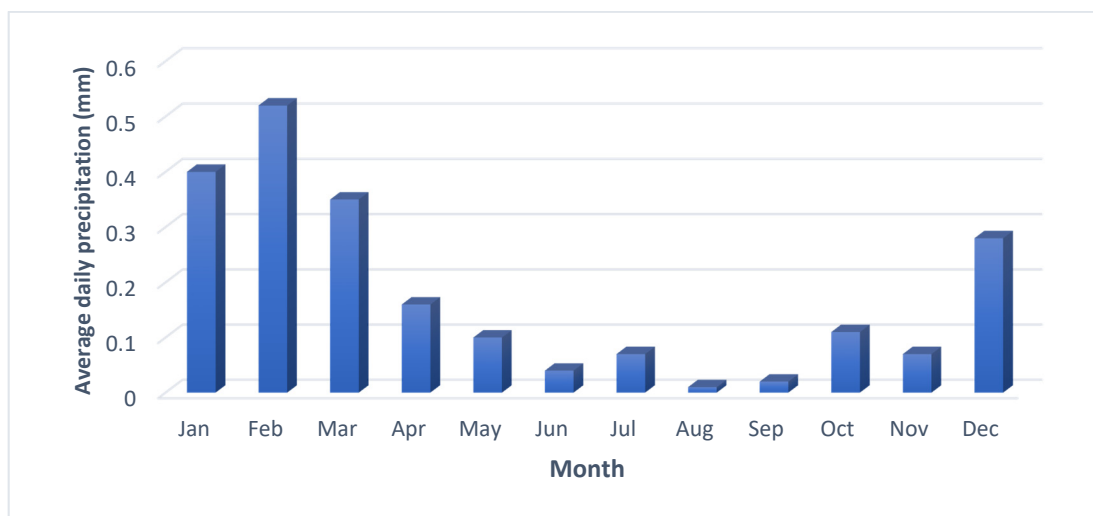

Figure 2. Average daily precipitation data collected from three meteorological stations in the Sistan and Baluchestan province based on the average values of the last 20 years [36].
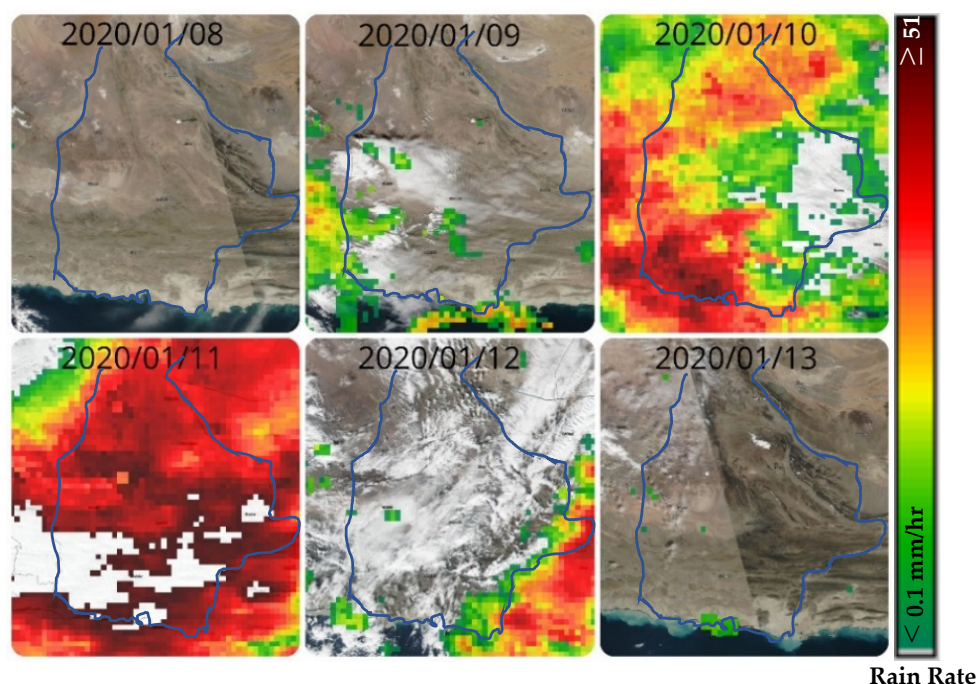
Figure 3. Rate of torrential precipitation in the Sistan and Baluchestan province over the period of six days from 8 January to 13 January, 2020. The maps were generated using the data provided by the authors of [37].

3. Data Set Description

3.1. CYGNSS data

There are three levels of CYGNSS data products in version 2.1, which represent the second post-provisional based on calibrated and validated level 1 algorithms. The level 1 (L1) dataset contains the measurement of surface Normalized Bistatic Radar Cross Section (NBRCS). The level 2 (L2) dataset includes derived ocean surface wind speed and Mean Square Slope (MSS). The level 3 (L3) dataset delivers hourly averaged wind speed and MSS on a 0.2 degree × 0.2 degree grid.

We used CYGNSS L1 data as the lowest level of the available data products. The format of the data is NetCDF (Network Common Data Form). Daily observations of each of the eight CYGNSS satellites are included in a NetCDF file. Accordingly, there are up to eight files for every Day Of a Year (DOY). The daily base data is available free of charge on the website of Physical Oceanography Distributed Active Archive Center (PO. DAAC) of NASA's Jet Propulsion Laboratory (JPL) at https://podaac.jpl.nasa.gov. Table 2 shows the main variables of the L1 data [24] which were used in this study.

Table 2. The Cyclone Global Navigation Satellite System (CYGNSS) data source parameters.

Parameters	Description
ddm_snr	Delay Doppler Map (DDM) signal-to-noise ratio, in dB
gps_tx_power_db_w	GPS transmit power, in dB.
rx_to_sp_range	Distance between the CYGNSS spacecraft and the specular point, in meters.
tx_to_sp_range	Distance between the GPS spacecraft and the specular point, in meters.
gps_ant_gain_db_i	GPS transmit antenna gain. Antenna gain in the direction of the specular point, in dBi
sp_rx_gain	Specular point Rx antenna gain. The receive antenna gains in the direction of the specular point, in decibel isotropic (dBi).
quality_flags	Per-DDM quality flags
sp_lat	Specular point latitude, in degrees North
sp_lon	Specular point longitude, in degrees East
sp_inc_angle	The specular point incidence angle, in degrees

3.2. Satellite Image

Moderate-Resolution Imaging Spectroradiometer (MODIS) is an advanced sensor on the Terra and Aqua Spacecraft for gathering data through a broad spectrum of electromagnetic waves. Terra was the first satellite of the Earth Observing System (EOS) program and was launched on 18 December, 1999. It passes north to south over the equator in the morning. Aqua is the second EOS satellite which carries a MODIS sensor and passes south to north across the equator in the afternoon. Terra and Aqua MODIS cover the Earth's surface every one to two days. The sensors onboard these satellites measure 36 spectral bands from 0.405 μm to 14.385 μm. The data is released by different resolutions, i.e., 250 m (bands 1–2), 500 m (bands 3–7), and 1000 m (bands 8–36). The MODIS data is accessible at https://modis.gsfc.nasa.gov and can be used for a significant number of applications in the land, atmosphere, and, ocean [38]. Figure 4 shows the false-color images of the Sistan and Baluchestan province (also regions of the Kerman and Hormozgan provinces) before the flood (A) and during the flood (B). The images were acquired by MODIS (bands 7–2–1) on 8 January and 13 January 2020. These images were used here for validation purposes.
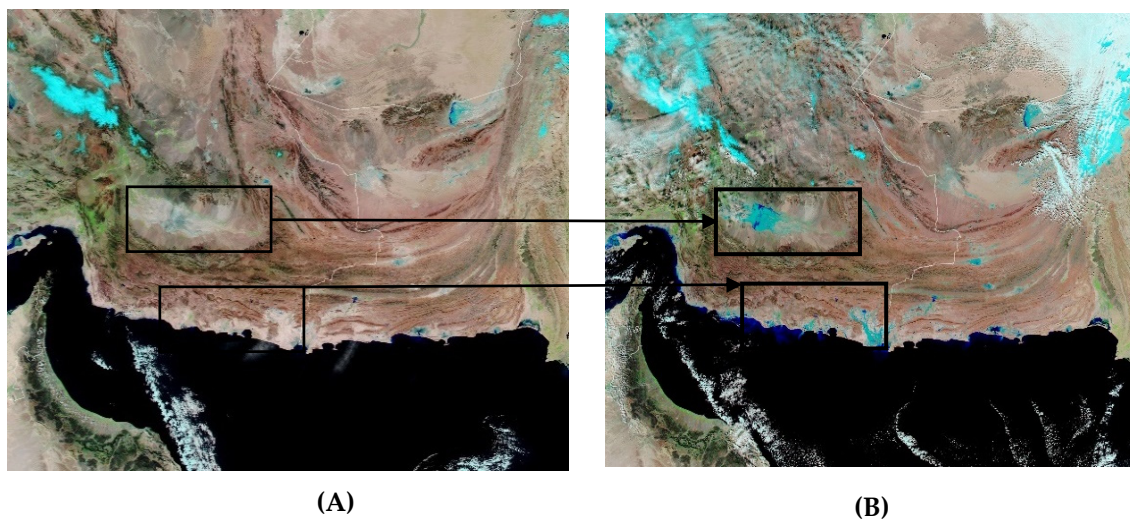

(A)　　　　　　　　　　　　　　　　　　　　　　　**(B)**

Figure 4. Moderate-Resolution Imaging Spectroradiometer (MODIS) images of the study area (**A**) before the flooding on 8 January 2020, and (**B**) during the flood on 13 January 2020. The dark blue regions are the inundated areas. The clouds in the image are shown with light blue which can be distinguished from the inundated areas [39].

4. Method and Discussion

The methodology in the current paper includes five main steps, as illustrated in Figure 5. The steps are: (1) Data collection, (2) data preparation, (3) calculating the surface reflectivity, (4) data calibration, and (5) flood detection and validation. Each step is described as follows.

4.1. The Bistatic Radar Equations

Radar is a system for detecting targets and deriving information such as position, velocity, and reflectivity signature from the detected objects [40]. It transmits a signal and receives the echo after it is reflected by a target. The types of radar systems based on the location of the transmitter (TX) and the receiver (RX) can be divided into colocated or monostatic radars, which measure backscattered signals, and separated or bistatic radars, which measure forward-scattered signals. The main difference between monostatic and bistatic radars is the separation of the transmitter and receiver [41]. Figure 6 shows monostatic and bistatic constellation for satellites.
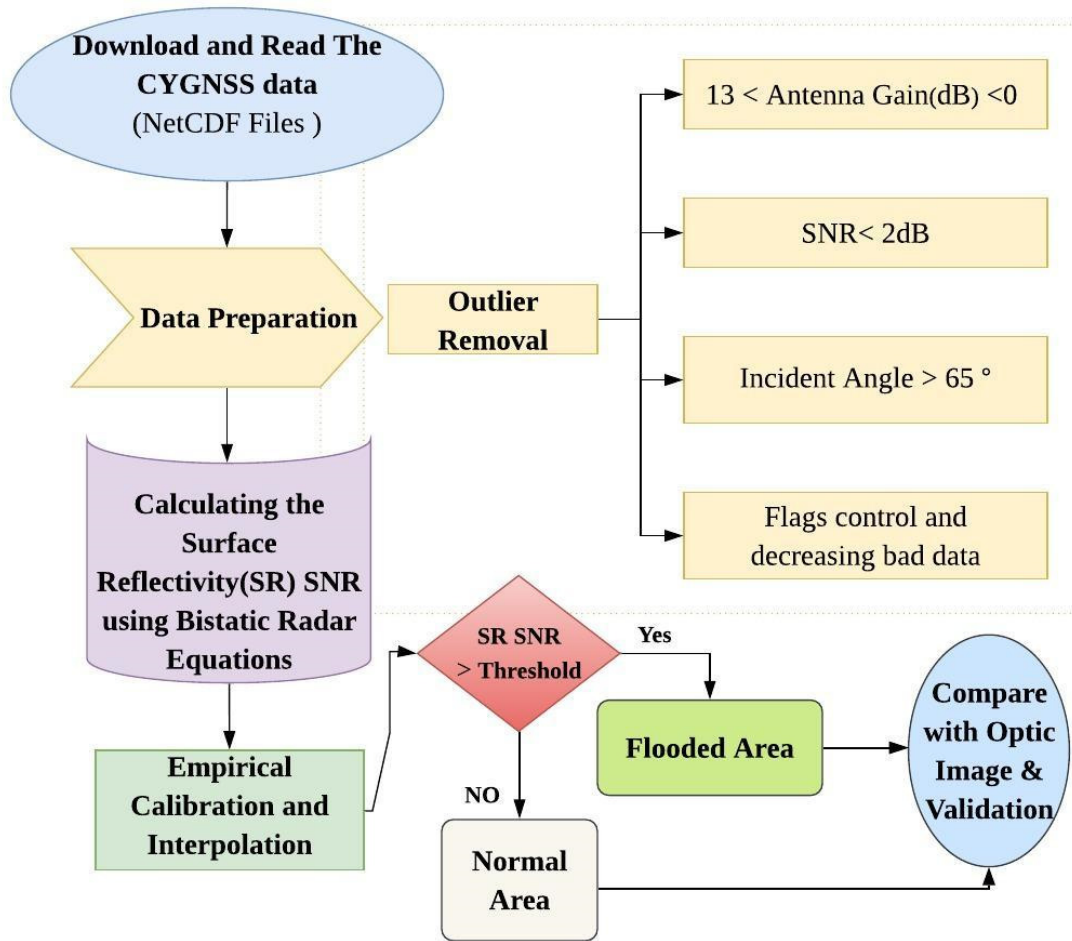
Figure 5. Methodology flowchart based on the bistatic radar concept and using CYGNSS data.
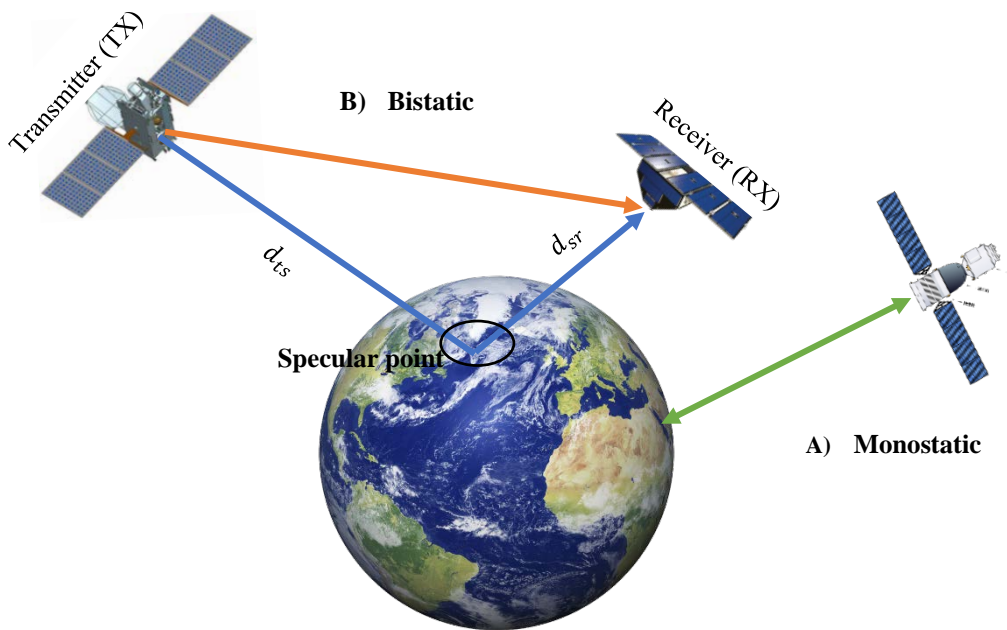

Figure 6. Simple schematic view of mono (**A**) and bistatic (**B**) radars constellation for satellite remote sensing.

The CYGNSS and GPS constellations form a bistatic radar system. The GPS satellites transmit circularly polarized microwave signals which are collected by the CYGNSS reflectometry receivers after forward-scattering from the Earth's surface. The scattered signals contain valuable information about the physical properties of the reflecting surface. Inland waters can be detected by CYGNSS, assuming a coherent forward-scattering mechanism [33,34,42]. The peak value of coherent scattered power is defined as [22,23,43]:

$$P_{RL}^{coh} = \frac{P_R^t \, G^t \, G^r}{(d_{ts} + d_{sr})^2} \left(\frac{\lambda}{4\pi}\right)^2 \Gamma_{RL} \qquad (1)$$

where P_{RL}^{coh} is the peak value of coherently received power, R denotes the right-handed circular polarization (RHCP) GPS transmit antenna, and L is related to the left-handed circular polarization (LHCP) of forward-scattered signals collected by the downward-looking antenna. P_R^t is the transmitted power, G^t is the gain of the transmitter antenna, G^r is the gain of the receiver antenna, λ is the GPS L1 wavelength (~0.19 m), and d_{ts} is the distance between the specular reflection point and the GPS transmitter, while d_{sr} is the distance between the specular reflection point and the GNSS-R receiver and Γ_{RL} is the surface reflectivity along with the incidence angle. In addition to the mentioned parameters P_{RL}^{coh} is affected by system noise. Therefore, signal-to-noise ratio (SNR) could be defined as:

$$SNR = \frac{P_{RL}^{coh}}{N} = \frac{P_R^t \, G^t \, G^r}{(d_{ts} + d_{sr})^2} \left(\frac{\lambda}{4\pi}\right)^2 \frac{\Gamma_{RL}}{N} \qquad (2)$$

where N is the noise value. Since the magnitude of the SNR is not equal to the reflected power, the surface reflectivity or corrected SNR along with the incidence angle could be computed using:

$$SNR_c = \frac{\Gamma_{RL}}{N} = SNR \frac{(d_{ts} + d_{sr})^2}{P_R^t G^t \, G^r} \left(\frac{4\pi}{\lambda}\right)^2 \qquad (3)$$

Finally, the SNR_c in decibel (dB) is:

$$SNR_{c\,dB} = SNR_{dB} + 10 \log\left(\frac{(d_{ts} + d_{sr})^2}{P_R^t G^t \, G^r} \left(\frac{4\pi}{\lambda}\right)^2\right) \qquad (4)$$

This parameter ($SNR_{c\,dB}$) is strongly related to the hydrological conditions of the land surface [18,34]. In this study, the following CYGNSS L1 variables were used for the calculation of the surface reflectivity:

- ddm_snr ($SNR_{dB} = 10 \log(S_{max}/N_{avg})$ with S_{max} being the maximum value in a single DDM bin and N_{avg} is the average raw noise counts per-bin
- gps_tx_power_db_w (P_R^t)
- gps_ant_gain_db_i (G^t)
- sp_rx_gain (G^r)
- rx_to_sp_range (d_{sr})
- tx_to_sp_range (d_{ts})

The parameter λ is the wavelength of the GPS L1 carrier (~0.19 m). We converted all the values to the dB scale (some of them were already in dB within the CYGNSS files).

4.2. Data Preparation and Calibration

Before and after using Equation (4), we employed several corrections and data editions and outlier identification as follows:

- GPS transmitter bias: GPS transmit powers are approximate estimates with some biases which should be considered. The main sources of these biases could be unknown transmitting powers of GPS satellites and the biases in P_R^t associated with GPS pseudorandom noise (PRN) codes [16,44]. We used empirical calibration developed by Chew et al. (2018) for CYGNSS products. Table 3 shows the magnitude of the biases which should be corrected during the estimation of $SNR_{c\ dB}$ [15].

- Incidence angle: This parameter also affects a coherent reflection when the incidence angles are above 40 degrees or 50 degrees and was negligible for our purpose [34], but we deleted data with an incidence angle of more than 65 degrees.

- Quality Control Flags: The Level 1A data product used in this study was refined by applying a set of quality control flags designed and included in the data to indicate potential problems [27,45]. The specific flags we used were 2, 4, 5, 8, 16, and 17, which were related to S-band transmitter powered up, spacecraft attitude error, black body DDM, DDM is a test pattern, the direct signal in DDM, and low confidence in the GPS EIR estimate, respectively. Based on the work by Chew et al. (2018) on soil moisture, we removed data with those quality flags in this study.

- Additional correction and removal: We removed data with SNR_{dB} less than 2dB and CYGNSS antenna gain of less than 0 dB or more than 13 dB. These corrections were empirical and are not standardized, but have been shown to be beneficial [16].

Table 3. Empirical biases in $SNR_{c\ dB}$ according to pseudorandom noise (PRN).

PRN	Bias (dB)	PRN	Bias (dB)	PRN	Bias (dB)	PRN	Bias (dB)
1	1.017	9	1.498	17	0.256	25	0.880
2	0.004	10	−0.783	18	−0.206	26	0.163
3	1.636	11	−0.230	19	−0.206	27	0.409
4	-	12	−1.021	20	0.345	28	−0.712
5	−0.610	13	0.007	21	−0.909	29	−1.032
6	0.24	14	−0.730	22	−0.838	30	0.877
7	−0.709	15	−0.376	23	−0.858	31	−0.562
8	0.605	16	−0.481	24	1.140	32	−0.819

Figure 7 shows the statistical information for corrected SNR using three days of CYGNSS data during the flood time. Figure 7A shows the calculated surface reflectivity SNR of CYGNSS tracks before (left side) and after (right side) the data preparation. As can be seen in the middle part of the figure, some of the measurements that may be misleading were removed. Figure 7B,C show the distribution of the measurements with respect to the incidence angle and antenna gain. Despite the fact that the data rectification procedure discarded about 48% of the observations, CYGNSS still provided enough data to detect the flood. The flooding period continued until 17 January 2020. We analyzed a dataset consisting of three days of CYGNSS observations to reduce the effect of losing a significant portion of the data.

4.3. Interpolation

An interpolation process was used here to retrieve a representative grid from the CYGNSS observation points. As shown in Figure 7A, the data derived from CYGNSS have irregular structures based on the satellite along-tracks. We used the natural neighbor interpolation method for gridding. The method was developed by Sibson [46] and is a multivariate interpolation according to Voronoi tessellation [47]. The principal formula is [48]:

$$G(x,y) = \sum_{i=1}^{N} w_i\, f(x_i, y_i) \tag{5}$$

where G is the estimated value at (x, y), $w_i = Q_k / R_k$ is the weights, and $f(x_i, y_i)$ is the known data at (x_i, y_i), R_k is the area of the initial Voronoi diagram element for point $P_k = (x_i, y_i)$. Q_k is the intersection

area of R_k and newly constructed element for the point (x, y). Therefore, the method algorithm is the algorithm to insert an additional point into the existing Voronoi diagram. Figure 8 illustrates the visual view of the natural neighbor interpolation method.
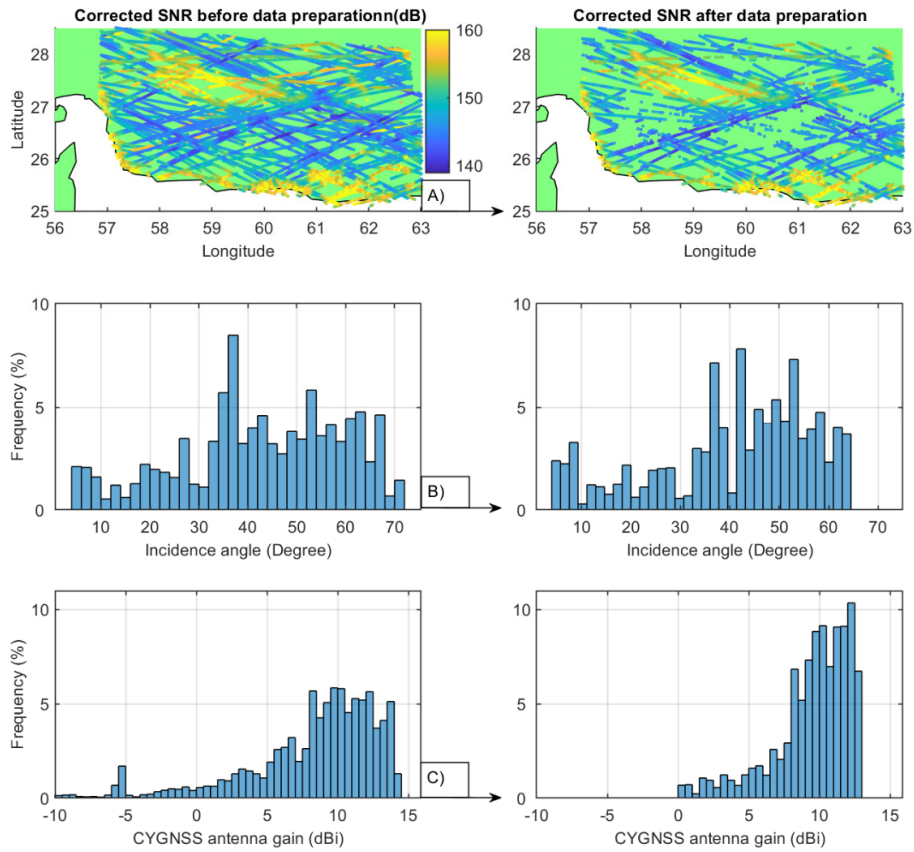

Figure 7. Statistical information of the data preparation step for the CYGNSS observations over a period of three days (13 January to 15 January 2020). (**A**) Corrected signal-to-noise ratio (SNR) before and after the preprocessing step. (**B,C**) The distribution of data according to incidence angle and antenna gain before and after data preparation.

Figure 8. The natural neighbor interpolation method. The area of the colored circles are the interpolating weights. The shaded area is a new Voronoi element for the point to be interpolated [48].

For CYGNSS data interpolation over our region of interest, we generated a grid with the resolution of 0.1° along the geodetic longitude and latitude and applied the mentioned interpolation method. Figure 9 shows the data before and after gridding. As can be seen from the figure, the gridded data is more sensible compared to the satellite tracks representation. Since *SNR* was not equal in magnitude to the $SNR_{c\ dB}$, the observations and corrections made in Equation (4) resulted in magnitudes greater than 140 dB (Figure 7A). To see the anomalies of the corrected $SNR_{c\ dB}$ in a visually reasonable range [11], 140 dB was subtracted from the original $SNR_{c\ dB}$ values.
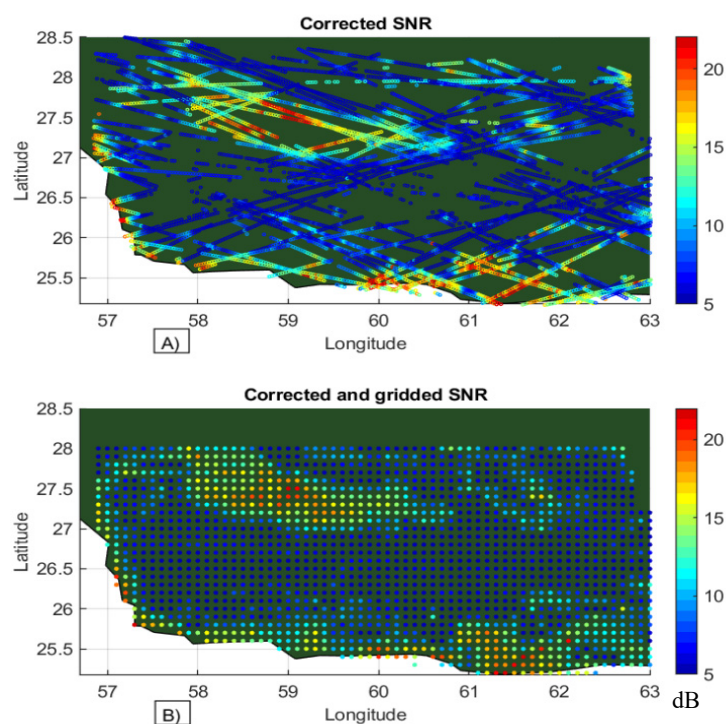
Figure 9. The outcome of the interpolation process for the corrected SNR ($SNR_{c\ dB}$) over the period of three days from 13 January to 15 January 2020. (**A**) Representation of the CYGNSS measurements along the satellite tracks, (**B**) the interpolated data at $0.1° \times 0.1°$ grid points using the natural neighbor interpolation method.

4.4. Evaluation and Mapping

As can be seen in Figure 4B, the flood happened in the south and middle part of the Sistan and Baluchestan province in Iran. Figure 10 shows the flooded regions which were detected by CYGNSS observations overlaid on the MODIS image (Figure 4B) for verification. The figure contains three regions with significant SNR anomalies. The regions are labeled A, B, and C.

Region A in Figure 10 belongs to the Hamun-Jaz Murian depression in the southeast of Iran, placed between the Kerman province and Sistan and Baluchestan province. The shape of the depression or basin is oblong and enclosed by the mountains. There is a seasonal lake, Hamun, in the middle of the basin, which has been dry through the recent dry years. Although the Halil and Bampur rivers are the main sources of feeding for the basin, neither of both bring significant water to the basin to fill this lake, because the water is used for agricultural purposes on the way [49,50]. Moreover, the recent flood in January 2020 was unique in terms of flood volume over the last decade. The previous flood in this region happened in June 2007. Figure 11 demonstrates the capability of CYGNSS measurements in the detection and mapping of the flood over this depression.

To calculate the flooded areas using corrected SNR, a threshold was used to distinguish inundated from noninundated areas. A simple threshold method has been used in previous studies with monostatic and bistatic radars [11,18]. As is seen in Figures 10–13, observations with the values greater than 11 dB corresponded to the flooded areas. This threshold was used for the detection of inundation in this study. This value could be different in other regions. The roughness and vegetation could weaken the signals and change the threshold. The threshold used by [11] was 12dB for the medium-vegetation density and typical roughness.

As can be distinguished from flooded areas in Figures 11 and 12, the values of corrected SNR more than 11 dB have a high correlation with the satellite image in the inundated region. However, minor discrepancies could be related to georeferencing or interpolation errors. The overall evaluation of the results using the three days of CYGNSS data reports an acceptable performance for flood detection.
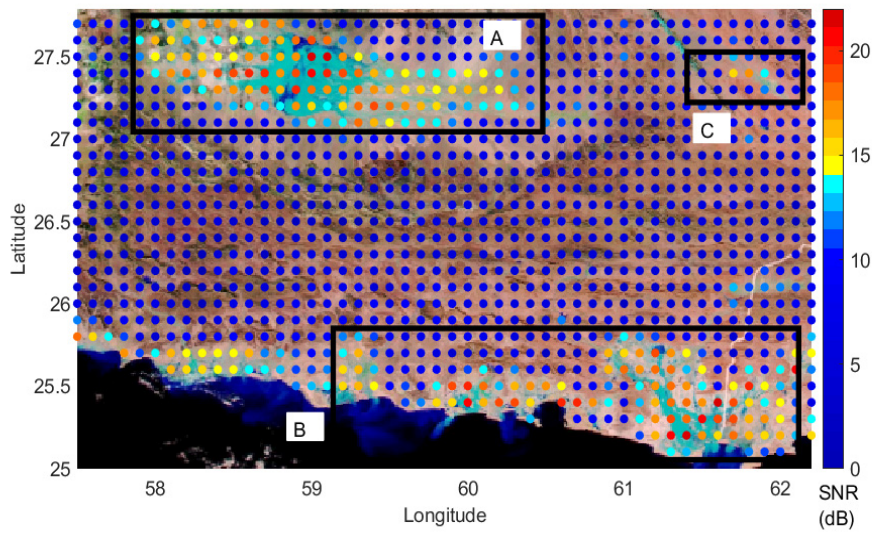
Figure 10. The georeferenced optical satellite imagery of the flood from MODIS (13 January 2020) overlaid by the corrected signal to noise ratio derived from CYGNSS observations (13 January to 15 January 2020). The regions labeled A, B, and C show significant SNR anomalies.
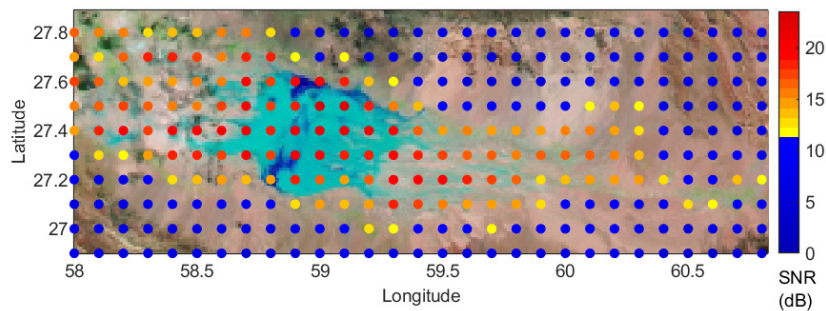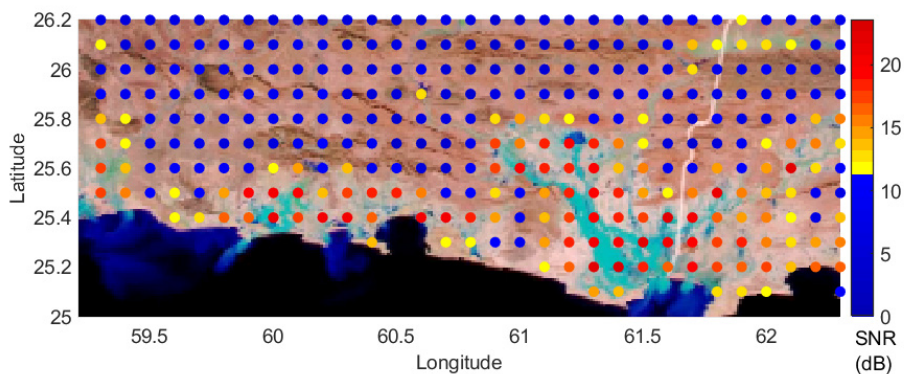

Figure 11. The georeferenced optical satellite imagery of the flood over the Hamun-Jaz Murian basin (region A in Figure 10) from MODIS (13 January 2020) overlaid by the corrected SNR derived from CYGNSS observations (13 January to 15 January 2020).

Figure 12. The georeferenced optical satellite imagery of the flood over coastlines and inundation of the nearby rivers (region B in Figure 10) from MODIS (13 January 2020) overlaid by the corrected SNR derived from CYGNSS observations (13 January to 15 January 2020).

Governments could use flood maps to establish the risk regions, safe evacuation options, and update the reaction plan. In the absence of promising and accurate flood maps, the development processes in or nearby the risk area are affected. The community lacks a tool to guide development to be more secure and to reduce future risks.
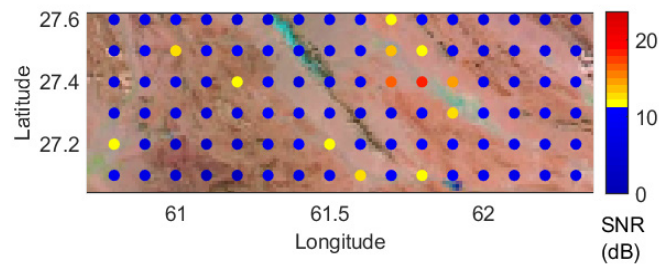
Figure 13. The georeferenced optical satellite imagery of the flood over the cities of Zaboli and Suran (region C in Figure 10) from MODIS (13 January 2020) overlaid by the corrected SNR derived from CYGNSS observations (13 January to 15 January 2020). The region includes a river and an inland water body.

We proceeded to map the detected inundation area. Google Maps was used here as an infrastructure which provides information about roads, cities, villages, etc. The derived data which shows flooded regions (data over 11 dB) was mapped on Google Maps. Figure 14 illustrates the three major regions of flood in Sistan and Baluchestan. Due to the flood in region A, corresponding to the Hamun-Jaz-Murian basin, the cities close to the basin, i.e., IranShahr, Eslam Abad, and Golmorti, and the roads between them, were affected. The area of this region is about 8706 square kilometers. Region B, which is close to the coastline and encompasses a few rivers, many cities, villages, farmlands, and roads, was also hit by the flood. The area of this region is about 9742 square kilometers. Region C, in close proximity to the region A, includes a river, an inland lake, and the cities Zaboli and Suran, which were affected. The area of this flooded region is about 1196 square kilometers. Therefore, based on the estimates from the CYGNSS observations, about 19644 square kilometers were affected by the flood in the south and middle parts of the Sistan and Baluchestan province. More severe impacts were seen in the regions close to the coastlines and nearby rivers.
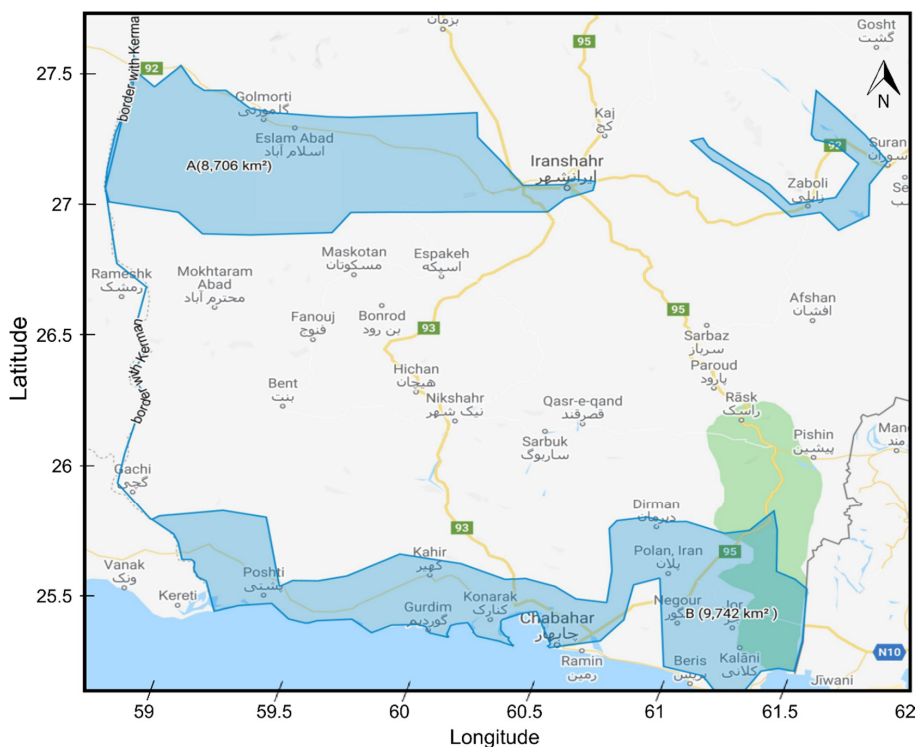

Figure 14. Map of the flooded regions laid over Google Maps. The blue-colored polygons show the boundary of the flooded areas, yellow lines are roads, and names of the cities are written on the map.

5. Summary and Conclusions

We applied the GNSS-R remote sensing technique based on a dataset of spaceborne observations of reflected GPS signals over the land to detect and map the recent flood in the southeastern part of Iran. The flood occurred in the Sistan and Baluchestan province after the heavy rain in mid-January 2020. The dataset used was acquired from the data products of the NASA CYGNSS mission. The main parameter of interest used in the analysis was the delay doppler map SNR, which was retrieved from the level-1 data product. First, a data preparation procedure was applied to remove outliers and discard low-quality data. In the next step, inverse bistatic radar formula was used to calculate the corrected SNR, which was closely related to surface reflectivity and hydrological conditions. The corrected SNR values were calibrated and interpolated to a regular grid over the study area. After calibration and gridding, the corrected SNR was verified with the MODIS optical image. A threshold of about 11 dB or more could be distinguished between the inundated and noninundated areas in the regions of interest. Finally, the flood-affected areas were mapped on Google Maps. The area of the flooded regions was estimated to be about 19,644 km^2 or 10.8% of the province. Many cities, roads, and other infrastructures were affected by the flood in these regions. The results indicate the regions close to depression, lakes, and coastal areas are at a high risk of flooding in this province. This study confirms that CYGNSS data is of value for hydrological investigations, particularly flood detection in the Sistan and Baluchestan province. Despite a relatively short revisit time of CYGNSS observations, the spatial resolution of the data products needs to be improved for mapping purposes. This issue could be addressed in future missions by, e.g., increasing the number of onboard processing channels, as well as by processing the reflected signals from other GNSS constellations such as GLONASS, Galileo, and BeiDou.

References

1. Van Westen, C. Remote sensing for natural disaster management. *Int. Arch. Photogramm. Remote Sens.* **2000**, *33*, 1609–1617.
2. Salami, R.O.; von Meding, J.K.; Giggins, H. Vulnerability of Human Settlements to Flood Risk in the Core Area of Ibadan Metropolis, Nigeria. *Jàmbá J. Disaster Risk Stud.* **2017**, *9*, 1–14. [CrossRef] [PubMed]
3. ADPC; UNDP. *Integrated Flood Risk Management in Asia*; A Primer ADPC: Bangkok, Thailand, 2005.
4. Abidin, H.Z.; Andreas, H.; Gumiar, I.; Sidiq, T.P.; Gamal, M. Environmental impacts of land subsidence in urban areas of Indonesia. In *FIG Working Week*; TS 3—Positioning and Measurement: Sofia, Bulgaria, 2015.
5. Nash, L.L. *The Colorado River Basin and Climatic Change: The Sensitivity of Streamflow and Water Supply to Variations in Temperature and Precipitation*; US Environmental Protection Agency, Office of Policy, Planning, and Evaluation: Washington, DC, USA, 1993.
6. Houston, J. Variability of precipitation in the Atacama Desert: Its causes and hydrological impact. *Int. J. Clim. J. R. Meteorol. Soc.* **2006**, *26*, 2181–2198. [CrossRef]
7. Brivio, P.A.; Colombo, R.; Maggi, M.; Tomasoni, R. Integration of remote sensing data and GIS for accurate mapping of flooded areas. *Int. J. Remote Sens.* **2002**, *23*, 429–441. [CrossRef]
8. CNN. Available online: https://edition.cnn.com/2019/04/07/middleeast/iran-flood-fatalities/index.html. (accessed on 7 April 2019).

9. Oberstadler, R.; Hönsch, H.; Huth, D. Assessment of the mapping capabilities of ERS-1 SAR data for flood mapping: A case study in Germany. *Hydrol. Process.* **1997**, *11*, 1415–1425. [CrossRef]

10. Kuenzer, C.; Guo, H.; Huth, J.; Leinenkugel, P.; Li, X.; Dech, S. Flood mapping and flood dynamics of the Mekong Delta: ENVISAT-ASAR-WSM based time series analyses. *Remote Sens.* **2013**, *5*, 687–715. [CrossRef]

11. Chew, C.; Reager, J.T.; Small, E. CYGNSS data map flood inundation during the 2017 Atlantic hurricane season. *Sci. Rep.* **2018**, *8*, 1–8. [CrossRef]

12. Rajabi, M.; Amiri-Simkooei, A.R.; Asgari, J.; Nafisi, V.; Kiaei, S. Analysis of TEC time series obtained from global ionospheric maps. *J. Geomat. Sci. Technol.* **2015**, *4*, 213–224.

13. Rajabi, M.; Amiri-Simkooei, A.R.; Nahavandchi, H.; Nafisi, V. Modeling and Prediction of Regular Ionospheric Variations and Deterministic Anomalies. *Remote Sens.* **2020**, *12*, 936. [CrossRef]

14. Tabibi, S. Snow Depth and Soil Moisture Retrieval Using SNR-Based GPS and GLONASS Multipath Reflectometry. Ph.D. Thesis, University of Luxembourg, Luxembourg, 2016.

15. Li, W.; Cardellach, E.; Fabra, F.; Rius, A.; Ribó, S.; Martín-Neira, M. First spaceborne phase altimetry over sea ice using TechDemoSat-1 GNSS-R signals. *Geophys. Res. Lett.* **2017**, *44*, 8369–8376. [CrossRef]

16. Chew, C.; Small, E. Soil moisture sensing using spaceborne GNSS reflections: Comparison of CYGNSS reflectivity to SMAP soil moisture. *Geophys. Res. Lett.* **2018**, *45*, 4049–4057. [CrossRef]

17. Wu, X.; Li, Y.; Xu, J. Theoretical study on GNSS-R vegetation biomass. In Proceedings of the 2012 IEEE International Geoscience and Remote Sensing Symposium, Munich, Germany, 12 November 2012.

18. Wan, W.; Liu, B.; Zeng, Z.; Chen, X. Using CYGNSS data to monitor China's flood inundation during typhoon and extreme precipitation events in 2017. *Remote Sens.* **2019**, *11*, 854. [CrossRef]

19. Hoseini, M.; Asgarimehr, M.; Zavorotny, V.; Nahavandchi, H.; Ruf, C.; Wickert, J. First evidence of mesoscale ocean eddies signature in GNSS reflectometry measurements. *Remote Sens.* **2020**, *12*, 542. [CrossRef]

20. Clarizia, M.P.; Ruf, C.S. Wind speed retrieval algorithm for the Cyclone Global Navigation Satellite System (CYGNSS) mission. *IEEE Trans. Geosci. Remote Sens.* **2016**, *54*, 4419–4432. [CrossRef]

21. Liu, B.; Wan, W.; Hong, Y. Can the Accuracy of Sea Surface Salinity Measurement Be Improved by Incorporating Spaceborne GNSS-Reflectometry? *IEEE Geosci. Remote Sens. Lett.* **2020**. [CrossRef]

22. Zavorotny, V.U.; Gleason, S.; Cardellach, E.; Camps, A. Tutorial on remote sensing using GNSS bistatic radar of opportunity. *IEEE Geosci. Remote Sens. Mag.* **2014**, *2*, 8–45. [CrossRef]

23. Eroglu, O.; Kurum, M.; Boyd, D.; Gurbuz, A.C. High Spatio-Temporal Resolution CYGNSS Soil Moisture Estimates Using Artificial Neural Networks. *Remote Sens.* **2019**, *11*, 2272. [CrossRef]

24. Teunissen, P.; Montenbruck, O. *Springer Handbook of Global Navigation Satellite Systems*; Springer: Cham, Switzerland, 2017.

25. Guerriero, L.; Pierdicca, N.; Egido, A.; Caparrini, M.; Paloscia, S.; Santi, E.; Floury, N. Modeling of the GNSS-R signal as a function of soil moisture and vegetation biomass. In Proceedings of the 2013 IEEE International Geoscience and Remote Sensing Symposium-IGARSS, Melbourne, VIC, Australia, 21–26 July 2013.

26. Masters, D.; Axelrad, P.; Katzberg, S. Initial results of land-reflected GPS bistatic radar measurements in SMEX02. *Remote Sens. Environ.* **2004**, *92*, 507–520. [CrossRef]

27. Ruf, C.; Chang, P.S.; Clarizia, M.P.; Gleason, S.; Jelenak, Z. *CYGNSS Handbook*; Michigan Pub: Ann Arbor, MI, USA, 2016; p. 154.

28. Ruf, C.S.; Atlas, R.; Chang, P.S.; Clarizia, M.P.; Garrison, J.; Gleason, S.; Katzberg, S.; Jelenak, Z.; Johnson, J.; Sharanya, J.; et al. New ocean winds satellite mission to probe hurricanes and tropical convection. *Bull. Am. Meteorol. Soc.* **2016**, *97*, 385–395. [CrossRef]

29. Ruf, C.S.; Chew, C.; Lang, T.; Morris, M.; Nave, K.; Ridley, A.; Balasubramaniam, R. A new paradigm in earth environmental monitoring with the CYGNSS small satellite constellation. *Sci. Rep.* **2018**, *8*, 1–13. [CrossRef]

30. Zribi, M.; Gorrab, A.; Baghdadi, N.; Lili-Chabaane, Z.; Mougenot, B. Influence of radar frequency on the relationship between bare surface soil moisture vertical profile and radar backscatter. *IEEE Geosci. Remote Sens. Lett.* **2013**, *11*, 848–852. [CrossRef]

31. Camps, A.; Park, H.; Pablos, M.; Foti, G.; Gommenginger, C.; Liu, P.W.; Jugge, J. Sensitivity of GNSS-R spaceborne observations to soil moisture and vegetation. *IEEE J. Sel. Top. Appl. Earth Obs. Remote Sens.* **2016**, *9*, 4730–4742. [CrossRef]

32. Chew, C.; Shah, R.; Zuffada, Z.; Hajj, G.; Masters, D.; Mannuci, A. Demonstrating soil moisture remote sensing with observations from the UK TechDemoSat-1 satellite mission. *Geophys. Res. Lett.* **2016**, *43*, 3317–3324. [CrossRef]

33. Gerlein-Safdi, C.; Ruf, C.S. A CYGNSS-based algorithm for the detection of inland waterbodies. *Geophys. Res. Lett.* **2019**, *46*, 12065–12072. [CrossRef]

34. Morris, M.; Chew, C.; Reager, J.; Shah, R.; Zuffada, C. A novel approach to monitoring wetland dynamics using CYGNSS: Everglades case study. *Remote Sens. Environ.* **2019**, *233*, 111417. [CrossRef]

35. Amineh, Z.B.A.; Hashemian, S.J.A.-D.; Magholi, A. Integrating Spatial Multi Criteria Decision Making (SMCDM) with Geographic Information Systems (GIS) for delineation of the most suitable areas for aquifer storage and recovery (ASR). *J. Hydrol.* **2017**, *551*, 577–595. [CrossRef]

36. World Data. Available online: https://www.worlddata.info (accessed on 1 February 2020).

37. Huffman, G.J.; Bolvin, D.T.; Nelkin, E.J. Integrated Multi-satellitE Retrievals for GPM (IMERG) technical documentation. *NASA/GSFC Code* **2015**, *612*, 47.

38. Lindsey, R.; Herring, D.; Abbott, M.; Conboy, B.; Esaias, W. *MODIS Brochure*; Goddard Space Flight Center: Greenbelt, MD, USA, 2013.

39. Flash Flooding in Iran. 2020. Available online: https://earthobservatory.nasa.gov/images/146150/flash-flooding-in-iran (accessed on 1 February 2020).

40. Eaves, J.L. Introduction to radar. In *Principles of Modern Radar*; Van Nostrand Reinhold; Springer: New York, NY, USA, 1987; pp. 1–27.

41. Bruder, J.A. IEEE Radar standards and the radar systems panel. *IEEE Aerosp. Electron. Syst. Mag.* **2013**, *28*, 19–22. [CrossRef]

42. Nghiem, S.V.; Zuffada, C.; Shah, R.; Chew, C.; Lowe, S.T.; Mannucci, A.J.; Cardellach, E.; Brakenridge, G.R.; Geller, G.; Rosenqvist, A. Wetland monitoring with global navigation satellite system reflectometry. *Earth Space Sci.* **2017**, *4*, 16–39. [CrossRef]

43. Masters, D. Surface Remote Sensing Applications of GNSS Bistatic Radar: Soil Moisture and Aircraft Altimetry. Ph.D. Thesis, University of Colorado, Boulder, CO, USA, 2004.

44. Wang, T.; Ruf, C.S.; Block, B.; McKague, D.; Gleason., S. Characterization of GPS L1 EIRP: Transmit power and antenna gain pattern. In Proceedings of the 31st ION GNSS, Miami, FL, USA, 24–28 September 2018.

45. Basis, A.T. Cyclone Global Navigation Satellite System (CYGNSS). Prepared by: Maria Paola Clarizia, University of Michigan, Valery Zavorotny, NOAA. 2015.

46. Sibson, R. *A Brief Description of Natural Neighbor Interpolation (Chapter 2)*; Barnett, V., Ed.; Interpolating Multivariate Data; John Wiley: Chichester, UK, 1981; pp. 21–36.

47. Voronoi, G. Nouvelles applications des paramètres continus à la théorie des formes quadratiques. Deuxième mémoire. Recherches sur les parallélloèdres primitifs. *J. für die reine und angewandte Mathematik (Crelles J.)* **1908**, *1908*, 198–287. [CrossRef]

48. Tsidaev, A. Parallel algorithm for natural neighbor interpolation. In Proceedings of the 2nd Ural Workshop on Parallel, Distributed, and Cloud Computing for Young Scientists, Yekaterinburg, Russia, 6 October 2016.

49. Harrison, J. The Jaz Murian depression, Persian Baluchistan. *Geogr. J.* **1943**, *101*, 206–225. [CrossRef]

50. Frs, N.F. From Musandam to the Iranian Makran. *Geogr. J.* **1975**, *141*, 55–58. [CrossRef]